University of Groningen

Top Master Programme in Nanoscience, Master thesis

Magnetic heat transport in MnF_2: dynamic measurement with fluorescent flash method

Qi Liu
Supervisors: Dr. Matteo Montagnese, Prof. Paul van Loosdrecht

July 2012

Abstract

Interplay of magnons and phonons was believed to give rise to interesting thermal properties in the classical antiferromagnet MnF_2. We employed fluorescent flash method to investigate the dynamic thermal transport in this material. Inspired by previous studies on low dimensional quantum magnets, we measured the thickness dependence of thermal diffusivities at both room temperature and below transition temperature. As expected, we observed a strong dependence of such only at low temperature. The behavior of such thickness dependence was attributed to the suggested very long magnon-phonon thermalization time τ_{mp}. Further studies can be done to further clarify this phenomenon and give a good estimation of τ_{mp}.

Contents

Chapter 1

Introduction

In low dimensional quantum antiferromagnets, for example single chain compound $SrCuO_2$ and spin ladder compound $Ca_9La_5Cu_{24}O_{41}$, magnetic excitations, or magnons, produce an important contribution to the thermal conductivities of the materials. Among these electronic insulator compounds, people have already found materials with large conductivities in one direction, while negligible in other directions. This phenomenon has potential applications in cooling systems in electronics structures where materials conducting heat but not electric current and anisotropic thermal conducting properties are quite neat.

Although magnons may have a very large thermal conductivity, the way they contributes to total thermal conductivity is by coupling to phonons. In fact experimentally only phonon system can be excited externally and measured directly. Magnons contribute only by exchanging heat with phonons. With different magnon-phonon coupling strengths, one can explain the great differences in certain 3D magnetic materials. Moreover, the thermalization time of magnon and phonon subsystems also give rise to a thickness dependence of thermal conductivities.

Magnon-phonon thermalization time can be measured directly by techniques such pulsed electron spin resonance experiments [1] and, more indirectly, by neutron scattering [2]. Also one can try to measure the thickness dependence of thermal conductivity, which demands much less cost. However, conventional steady state conductivity measurements have difficulties measuring thin samples due to technical hindrances. A dynamical way to measure the bulk thermal conductivity on thin sample is the flash method [3].

In flash method measurement, a short laser pulse was applied to one side of a rod-like sample, and the temperature change versus time of the other side of the sample is measured. The resulting transient curve enables one to extract thermal conductivities. In this project, we use one particular version of this method, the fluorescent flash method, where the temperature detector is a thin layer of fluorescent material deposited onto the measured surface.

In previous works, we found that the dynamically measured thermal conductivities of spin chain compounds are 2 times smaller compared to steady state measurements. We came up with a model where broken spin chains inside a sample with reduce the dynamic thermal conductivity, but have no effect on steady state conductivity. To make sure that these dynamic measurements are truly reliable, a test magnetic material was chosen to benchmark the method. We selected manganese fluoride, MnF_2, because it's a very well studied 3D antiferromagnetic compound and has a very long magnon-phonon thermalization time.

Another purpose of this project is to measure the magnon-phonon thermalization time constant for single crystalline MnF2 and compare our results with literature values. To get there, we need to measure the thermal conductivities of samples of different thicknesses.

The outlines of this thesis is as follows.

- Chapter 2, theory of heat conduction is reviewed.
- Chapter 3, principles of the measurement method is introduced and key facts concerning our experiments are outlined.
- Chapter 4, results of measurement on MnF_2 is displayed and discussed. Conclusions of current situation and outlooks of further studies are suggested.

Chapter 2

Theoretical considerations

2.1 Heat conduction equation

Heat transport is the evolution of temperature distribution over time in certain material, resulting from the random thermal motion, or diffusion, of particles which carry the thermal energy. The diffusion of thermal energy inside a material is governed by the heat equation.

The temperature of a system is defined proportional to the average kinetic energy of the particles in the system, e.g. phonons in a solid. For most cases, the smallest size of a system whose temperature can be well-defined is macroscopically speaking infinitesimal. Thus one can treat the temperature distribution inside a piece of solid as a continuous function of position $\mathbf{r}$ and time t, $T = T(\mathbf{r}, t)$.

It is assumed that at a given time and position, the heat flux density $\mathbf{f}(\mathbf{r}, t)$ which is the amount of energy flowing through unit area around the point $\mathbf{r}$ in unit time $\mathbf{f} = \frac{\mathrm{d}\mathbf{Q}}{\mathrm{d}t}$, is proportional to the local temperature gradient ∇T,

$$\mathbf{f}(\mathbf{r}, t) = -\kappa \nabla T(\mathbf{r}, t)\,, \tag{2.1}$$

where κ is defined as the thermal conductivity. This is called the law of heat conduction, also known as the Fourier's law. Fourier's law is originally an empirical law derived from measurements, and also can be derived from linear response theory [4]. Similar equations can be written down for other diffusion processes, e.g. Fick's law of diffusion for particle diffusion.

In general, conductivity is a tensor, $\boldsymbol{\kappa} = (\kappa_{ij})$, where $i, j = x, y, z$. One can diagonalize the matrix by choosing coordinate axes as the crystal axes of the material. For a uniaxial crystal

the thermal conductivity takes the form

$$\boldsymbol{\kappa} = \begin{pmatrix} \kappa_\perp & & \\ & \kappa_\perp & \\ & & \kappa_\parallel \end{pmatrix} , \tag{2.2}$$

where $\kappa_\perp$ and $\kappa_\parallel$ are the conductivities perpendicular and parallel to the crystal axis (usually c direction) respectively. For arbitrary crystal orientation with respect to the reference frame, transformation of thermal conductivity tensor is straightforward, $\boldsymbol{\kappa}' = \mathbf{R}^{\mathrm{T}} \boldsymbol{\kappa}\, \mathbf{R}$, where $\mathbf{R}$ is the rotation matrix from crystal axes to coordinate axes [5]. This property is similar to the dielectric constant tensor of a uniaxial birefringent crystal.

Since thermal conductivity is a local property, it's a function of position as well as temperature, $\boldsymbol{\kappa} = \boldsymbol{\kappa}(\mathbf{r}, T)$. When one is considering a homogeneous material, thermal conductivity tensor is instead independent of position $\boldsymbol{\kappa} = \boldsymbol{\kappa}(T)$. For the simplest case, i.e. in a homogeneous and isotropic medium, thermal conductivity is a scalar function of temperature only $\boldsymbol{\kappa} = \kappa(T)$.

Based on Fourier's law, one can derive heat equation from energy conservation. The energy flow into a unit volume in unit time is given by minus divergence of the heat flux, $\mathrm{d}E = -\nabla \cdot \nabla \mathbf{f}\, \mathrm{d}V\, \mathrm{d}t$, causing the temperature change $\mathrm{d}T$ in such volume if no heat is produced in such volume. This gives

$$C\, \mathrm{d}V\, \mathrm{d}T = -\nabla \cdot \nabla \mathbf{f}\, \mathrm{d}V\, \mathrm{d}t\,,$$

where ρ is the mass density and C the heat capacity per unit volume. Using Fourier's law (2.1) one can then get the heat equation,

$$C\, \frac{\partial T}{\partial t} - \nabla \cdot (\boldsymbol{\kappa}\, \nabla T) = 0\,. \tag{2.3}$$

For a one dimensional heat conduction problem, e.g. an homogeneous rod-like sample where heat diffusion happens along the axis while within the cross section temperature does not vary, if one consider very small temperature change or treating κ as a constant, equation 2.3 becomes

$$C\, \frac{\partial T}{\partial t} - \kappa \frac{\partial^2 T}{\partial x^2} = 0\,. \tag{2.4}$$

κ here then represents the thermal conductivity of the material along the heat transport direction. For isotropic materials, this value is the same with different direction, while in some materials, thermal conductivities can be greatly different for different heat transport directions. This also enlightens people to investigate thermal rectifiers where one can have large conductivity while in another direction it's almost thermally insulating. For crystals with conductivity tensor in the form of equation 2.2, thermal conductivity along an arbitrary direction is given by

$$\kappa_\theta = \sin^2\theta\, \kappa_\perp + \cos^2\theta\, \kappa_\parallel\,, \tag{2.5}$$

where θ is the angle between heat transport direction and c axis of the crystal [5]. For example, for heat transport in the (101) direction (45° from c and from a axes), thermal conductivity is $\kappa_{45^\circ} = \frac{1}{2}(\kappa_\perp + \kappa_\parallel)$. Using equation 2.5 one can in principle determine the orientation of crystal axes by measuring thermal conductivities along two different directions, given the values $\kappa_\perp$ and $\kappa_\parallel$. Of course thermal conductivity measurements are in general not very accurate compared to e.g. birefringence measurements.

2.2 One dimensional heat flow problem

For one dimensional heat transport in a slab or rod like solid with two parallel faces between $x = 0$ and $x = L$, one can rewrite equation 2.4 as the following

$$\frac{\partial T}{\partial t} - \alpha \frac{\partial^2 T}{\partial x^2} = 0\,, \tag{2.6}$$

where

$$\alpha = \frac{\kappa}{C} \tag{2.7}$$

is called thermal diffusivity or heat diffusion constant. Heat diffusivity is the only parameter in heat diffusion equation, just like diffusion constant for particle diffusion problems. Analytical solutions to equation 2.6 have been worked out under several different boundary conditions, with diffusivity α taken as a constant.

2.2.1 Steady state solution

For steady state temperature distribution, temperature at each position doesn't vary with time, $\partial T/\partial t = 0$, thus

$$\frac{\partial^2 T}{\partial x^2} = 0\,.$$

The solution is a linear function

$$T(x) = \frac{T_L - T_0}{L} x + T_0\,,$$

where $T_L = T(x = L)$ and $T_0 = T(x = 0)$ are boundary temperatures. For insulating boundary conditions, which means the temperature gradients at both ends are zero, $\partial T/\partial x|_{x=0,L} = 0$, this leads to the obvious solution $T(x)$ =constant. For the boundary condition where two ends kept at different constant temperatures, the temperature distribution is a line connecting two end point temperatures. In this case the heat flux at each point is given by

$$f = -\kappa \frac{\partial T}{\partial x} = \kappa \frac{T_0 - T_L}{L} = \text{constant}\,.$$

This shows a static state way to measure thermal conductivity, namely keeping one end of the sample contact with a heat sink with temperature, while heating the other end with constant heat flux f (e.g. constant heating power), then measuring the temperature drop ΔT over a distant ΔL of the sample. Then one can extract thermal conductivity by

$$\kappa_{\text{static}} = f \left| \frac{\Delta L}{\Delta T} \right| . \tag{2.8}$$

For such kinds of measurements, the stability of the input power would be crucial. Also it would be difficult to measure very small samples, since non-interfering temperature measurement within small spatial distance is not easy to achieve.

2.2.2 Dynamical situation

Generally one has to solve the heat equation 2.6 under different boundary conditions and initial temperature distribution. Notice that the eigenfunctions for such heat diffusion equation are in the form

$$T_\lambda(x,t) = (A_\lambda \sin \lambda x + B_\lambda \cos \lambda x) \exp(-\lambda^2 \alpha t) .$$

where λ is the corresponding eigenvalue, A_λ and B_λ are constants. One can use such eigenfunctions as bases to construct solutions for different situations.

For thermally insulating boundary condition $\partial T/\partial x|_{x=0,L} = 0$ and initial temperature distribution as $T(x,0) = u(x)$, the solution is given by [6]

$$T(x,t) = \frac{1}{L}\int_0^L u(x')\,\mathrm{d}x' + \frac{2}{L}\sum_{n=1}^{\infty} \exp\left(-\frac{n^2\pi^2\alpha t}{L^2}\right) \cos\frac{n\pi x}{L} \int_0^L u(x') \cos\frac{n\pi x'}{L}\mathrm{d}x' \tag{2.9}$$

When a laser pulse with energy density Q (in J/m^2) is heating up the front surface $x = 0$ of a slab shaped sample with uniform base temperature T_0, we can approximate the initial temperature profile with a step function showing one thin layer with thickness g near the front side uniformly heated,

$$T(x,0) \simeq \begin{cases} \frac{Q}{Cg} + T_0, & \text{for } 0 < x < g\,, \\ T_0, & \text{for } g < x < L\,. \end{cases}$$

For convenience, from now on we set T_0 as the zero temperature. Substituting such initial condition into the general solution 2.9, one gets

$$T(x,t) = \frac{Q}{CL}\left[1 + 2\sum_{n=1}^{\infty} \cos\frac{n\pi x}{L} \frac{\sin(n\pi g/L)}{n\pi g/L} \exp\left(-\frac{n^2\pi^2\alpha}{L^2}t\right)\right] . \tag{2.10}$$

In the summation, usually including a few terms is enough to depict the true solution. By also considering the penetration depth g is usually very small compared sample thickness L, one can

write $\sin(n\pi g/L) \simeq n\pi g/L$, thus the parameter g vanishes in the expression, which in turn also supports that the solution does not depend strongly on this parameter. For the rare surface $x = L$, using such approximation, the temperature over time is given by

$$T(L,t) = \frac{Q}{CL}\left[1 + 2\sum_{n=1}^{\infty}(-1)^n \exp\left(\frac{-n^2\pi^2\alpha}{L^2}t\right)\right]. \tag{2.11}$$

This is called Parker's formula [3]. A plot of this function is shown in Figure 2.1. When such

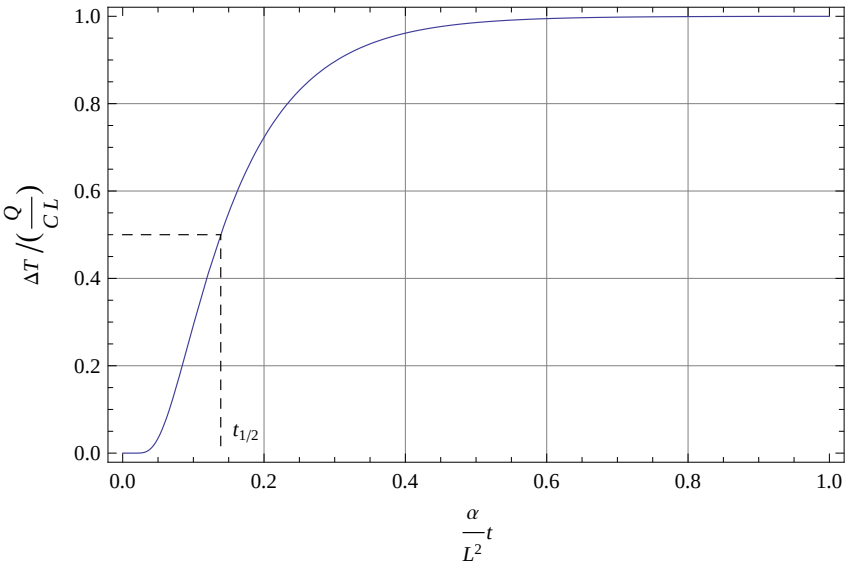

Figure 2.1: Parker's formula, showing normalized temperature against normalized time.

a curve is produced in experiments, e.g. in laser flash method measurements, one can extract thermal diffusivity as well as heat capacity from the curve. Notice that the temperature rise due to input laser pulse, $\Delta T_{\max} = Q/(CL)$, thus heat capacity is given by

$$C = \frac{Q}{L\Delta T_{\max}}. \tag{2.12}$$

For thermal diffusivity, one simple way is to determine the "half time" $t_{\frac{1}{2}}$ when the temperature rise ΔT reaches 50% of the maximum. The half time is calculated to be $\alpha t_{\frac{1}{2}}/L^2 \simeq 0.139$, so thermal diffusivity is given by

$$\alpha = 0.139L^2 \Big/ t_{\frac{1}{2}}\ . \tag{2.13}$$

2.3 Two temperature model

In magnetic insulators, heat is transport is done by phonons as well as magnons. The coupling between phonon and magnon subsystems can be described by a two temperature model. In this

model, phonon and magnon subsystems have different temperatures, T_l for phonons (lattice) and T_m for magnons (spins).

We follow the derivation from Sanders and Walton 1976 paper [7]. In a thermally isolated system, the magnon temperature should eventually come to equilibrium with phonon temperature characterized by a time constant known as magnon-phonon thermal relaxation time τ_{mp}. τ_{mp} can be defined using the following equation

$$\frac{\mathrm{d}}{\mathrm{d}t}\Delta T = -\frac{\Delta T}{\tau_{\mathrm{mp}}}\,, \tag{2.14}$$

where $\Delta T = T_l - T_m$ is the temperature difference between phonon and magnon subsystems. Using energy conservation, one can get

$$\frac{\mathrm{d}T_l}{\mathrm{d}t} = \frac{C_m}{C_l + C_m}\frac{T_m - T_l}{\tau_{\mathrm{mp}}}\,, \tag{2.15a}$$

$$\frac{\mathrm{d}T_m}{\mathrm{d}t} = \frac{C_l}{C_l + C_m}\frac{T_l - T_m}{\tau_{\mathrm{mp}}}\,, \tag{2.15b}$$

where C_l and C_m are the specific heats (heat capacity per unit volume) of phonon and magnon subsystems respectively.

To derive the heat diffusion equation for phonon and magnon subsystems in a one dimensional problem, one can combine equation 2.15 and 2.6, resulting

$$\frac{\partial T_l}{\partial t} = \alpha_l \frac{\partial^2 T_l}{\partial x^2} - g_l(T_l - T_m)\,, \tag{2.16a}$$

$$\frac{\partial T_m}{\partial t} = \alpha_m \frac{\partial^2 T_m}{\partial x^2} + g_m(T_l - T_m)\,, \tag{2.16b}$$

where

$$g_l = \frac{C_m}{C_l + C_m}\frac{1}{\tau_{\mathrm{mp}}}\,, \quad g_m = \frac{C_l}{C_l + C_m}\frac{1}{\tau_{\mathrm{mp}}}$$

are the coupling constants.

2.3.1 Steady state solution

The steady state temperature distributions $T_l(x)$ and $T_m(x)$, since $\partial T/\partial t = 0$, equations 2.16 can be written as

$$\kappa_l \frac{\mathrm{d}^2 T_l}{\mathrm{d}x^2} - g(T_l - T_m) = 0\,, \tag{2.17a}$$

$$\kappa_m \frac{\mathrm{d}^2 T_m}{\mathrm{d}x^2} + g(T_l - T_m) = 0\,, \tag{2.17b}$$

where coupling constant g is given by

$$g = \frac{C_m C_l}{C_l + C_m}\frac{1}{\tau_{\mathrm{mp}}}\,.$$

If one introduces the boundary conditions as constant heat flux Q propagating through the sample $x \in [-L/2, L/2]$, then the following is true:

$$Q = -\kappa_l \frac{\mathrm{d}T_l(x)}{\mathrm{d}x} - \kappa_m \frac{\mathrm{d}T_m(x)}{\mathrm{d}x} \,.$$

This means

$$\kappa_l T_l(x) + \kappa_m T_m(x) = -Qx + \text{contant} \,.$$

If one consider the center point $x = 0$, phonon and magnon temperature should both be the average temperature of the sample due to symmetry consideration,

$$T_l(0) = T_m(0) = T_0 \,.$$

Then

$$\kappa_l T_l(x) + \kappa_m T_m(x) = -Qx + (\kappa_l + \kappa_m) T_0 \,. \tag{2.18}$$

Another important part of the boundary conditions is the thermal insulating conditions at both ends,

$$\left.\frac{\mathrm{d}T_m}{\mathrm{d}x}\right|_{x=\pm L/2} = 0 \,. \tag{2.19}$$

Thus the magnon temperature can be solved by combining equations 2.17, 2.18 and 2.19, giving

$$T_l(x) = T_0 - \frac{Q}{\kappa_l + \kappa_m} \left(x + \frac{\kappa_m}{\kappa_l} \frac{\sinh Ax}{A \cosh \frac{1}{2} AL} \right) , \tag{2.20a}$$

$$T_m(x) = T_0 - \frac{Q}{\kappa_l + \kappa_m} \left(x - \frac{\sinh Ax}{A \cosh \frac{1}{2} AL} \right) , \tag{2.20b}$$

where

$$A = \left(\frac{C_l C_m}{C_l + C_m} \frac{\kappa_l + \kappa_m}{\kappa_m \kappa_l} \frac{1}{\tau_{\mathrm{mp}}} \right)^{1/2} . \tag{2.21}$$

For perfectly coupled magnons and phonons, the relaxation time is zero $\tau_{\mathrm{mp}} \to 0$, then $A \to \infty$. In this case magnon and phonon subsystems have the the same temperature distribution

$$T_l(x),\, T_m(x) \to T_0 - \frac{Q}{\kappa_l + \kappa_m} x \,.$$

While in the other limit, i.e. magnons and phonons are completely decoupled, $\tau_{\mathrm{mp}} \to \infty$, then $A \to 0$, then the temperature distributions are

$$T_l(x) \to T_0 - \frac{Q}{\kappa_l} x \,, \text{ and } T_m(x) \to T_0 \,.$$

In this case the magnon system is not thermally excited and no temperature gradient over the sample. Thus heat is only carried by phonons no matter how large the intrinsic magnon thermal conductivity is.

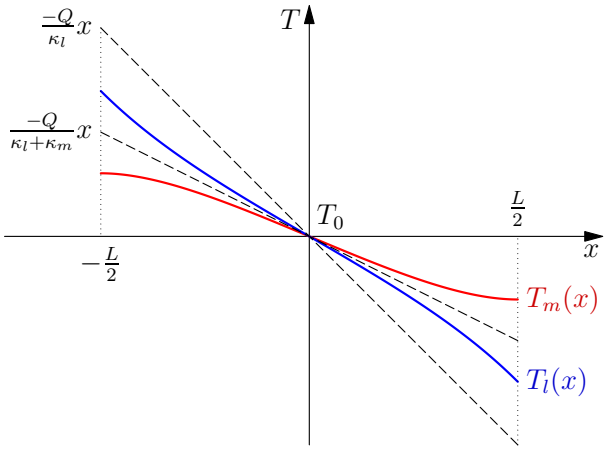

Figure 2.2: Typical solutions for magnon temperature $T_m(x)$ (in blue) and phonon temperature $T_l(x)$ (in red) using parameters $AL = 5$ and $\kappa_m/\kappa_l = 1$. Two limiting cases, where $\tau_{\text{mp}} \to 0$ or ∞, are plot in dashed lines.

A plot for typical solutions of $T_l(x)$ and $T_m(x)$ is depicted in figure 2.2.

For thermal conductivity measurements, usually only phonon temperature is available by for example thermal couples or infrared temperature sensor, so one obtains a temperature difference at two ends as

$$\Delta T_{\text{eff}} = \Delta T_l = T_l(L/2) - T_l(-L/2)\,.$$

Thus the effective thermal conductivity from measurements is given by

$$\kappa_{\text{eff, static}} = -\frac{QL}{\Delta T_{\text{eff}}} = (\kappa_l + \kappa_m) \Bigg/ \left(1 + \frac{\kappa_m}{\kappa_l}\frac{\tanh \frac{1}{2}AL}{\frac{1}{2}AL}\right)\,. \tag{2.22}$$

As we can see from this expression, if magnon-phonon thermalization time is very short, $A \to \infty$ so $\kappa_{\text{eff}} \to \kappa_l + \kappa_m$, the measured thermal conductivity equals to the sum of magnon and phonon conductivities. While in the other limit where relaxation time is very long, $A \to 0$ so $\kappa_{\text{eff}} \to \kappa_l$, the measured thermal conductivity is just that of phonons. One can also draw from this expression that the measured thermal conductivity of a particular material depends on the thickness of the sample. A plot of expression 2.22 as a function of parameter AL is show in figure 2.3.

2.3.2 Dynamic situation

For dynamic solution of heat conduction problem in the two-temperature model, the measured or effective thermal conductivity is given by a similar expression,

$$\kappa_{\text{eff, dynamic}} = (\kappa_l + \kappa_m) \Bigg/ \left(1 + \frac{\kappa_m}{\kappa_l}\frac{\tanh\left(\frac{1}{2}AL\right)^2}{\left(\frac{1}{2}AL\right)^2}\right)\,. \tag{2.23}$$

The relation between this dynamic effective conductivity is similar to static case. A curve showing the thickness dependence is also plotted in figure 2.3. Notably different from static results is that dynamic effective conductivity approaches to a plateau value at smaller thickness.

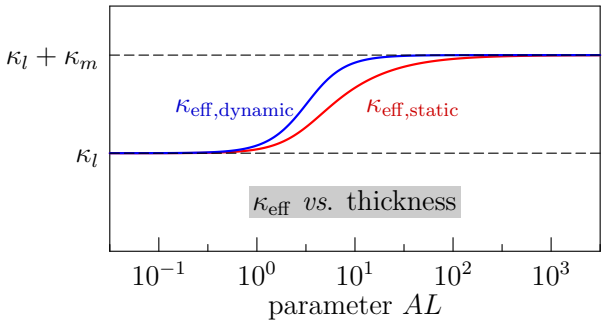

Figure 2.3: Effective thermal conductivity κ_{eff} calculated from two-temperature model as a function of parameter AL for both static situation (red) and dynamic situation (blue). In both cases, for short relaxation time or large thickness, κ_{eff} approaches the sum of magnon and phonon thermal conductivities $\kappa_l + \kappa_m$; for long relaxation time or small thickness, κ_{eff} approaches κ_l. Compared to static effective conductivity, the dynamic one increases faster as thickness increases, and reaches the plateau at nearly an order of magnitude smaller thickness.

2.4 Hypothesis for observed anomaly

Two temperature model successfully formulates a thickness dependence of measured thermal conductivity, but it can not explain the anomaly observed in dynamic thermal conductivity measurement spin ladder compound $Ca_9La_5Cu_{24}O_{41}$ where the plateau value is only rough half the steady state measurement result.

The anomaly in dynamic measurements can be explained qualitatively by a "broken chain" model [8]. In these spin chain and spin ladder samples, there are for sure impurities, meaning broken chains and ladders along c direction. At these broken spots, magnons from two sides are separated, thus no direct heat exchange between the two parts. The thermal contact between these two parts is the phonons. If magnon-phonon coupling is fast, the phonons in between two magnon parts act as a good thermal contact; while if magnons and phonons are coupled weakly, the two magnon parts are thermally isolated. So if the material has a long magnon phonon thermalization time, the macroscopic dynamic conductivity will be limited by the broken chains, resulting in much smaller conductivity. These broken links do not affect the steady state conductivity because there magnons and phonons are already in their equilibrium, thus no fast coupling between the two carriers is required.

Chapter 3

Materials and Methods

3.1 MnF_2

3.1.1 Basic properties

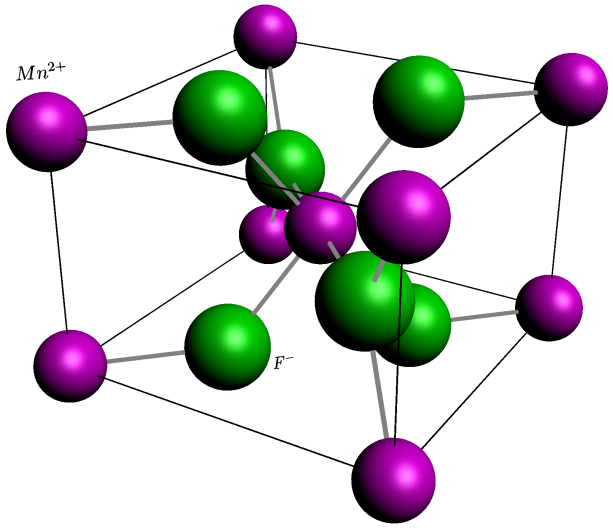

Figure 3.1: Unit cell structure of MnF_2. Magenta spheres represent Mn^{2+} ions sitting at corners and body center, green spheres F^-.

Manganese fluoride is a 3-dimensional antiferromagnetic salt, the critical temperature of its paramagnetic-antiferromagnetic transition is T_N =67.3 K [9] but no structural change [10]. Its unit cell, illustrated in figure 3.1, is a tetragonal rutile structure which belongs to space group $P4_2/mnm$ (D_{4h}^{14}). The lattice constants at room temperature are $a = b = 4.87$ Å, $c = 3.31$ Å, and the structural parameter $u = 0.310$ [11]. The room temperature mass density is $\rho = 3.93\,\mathrm{g \cdot cm^{-3}}$ [10].

Mn^{2+} ion has electron configuration $3d^5$ and in a high spin state with spin $S = 5/2$. Two next nearest neighboring manganese ions (a center one and a corner one) have antiferromagnetic superexchange interaction with each other through a nearest neighboring fluoride ion. Below Néel temperature in the antiferromagnet phase, nearest neighboring Mn^{2+} ions have oppositely aligned spins, with the preferred alignment in $\pm c$ direction [12].

It's a birefringent crystal with refractive index difference $\Delta n = 0.029$ for 632 nm light, and this birefringence is temperature and magnetic field dependent [13, 14]. Raman spectra of phonons as well as magnons (low temperature) can be found in references [15, 16].

3.1.2 Thermal properties

The heat capacity of MnF_2 at different temperatures is given in reference [9], and re-plot in figure 3.2a. As shown in the figure, there is a peak around with the phase transition temperature 67.3 K, in addition to a monotonically increasing baseline. The peak is assigned to magnon heat capacity, while the baseline corresponds to phonon heat capacity [9, 17]. The result is that only near and below transition temperature, magnon heat capacity is comparable to that of phonon, at temperatures far away from T_N, contribution of magnons can be neglected, as shown in figure 3.2b.

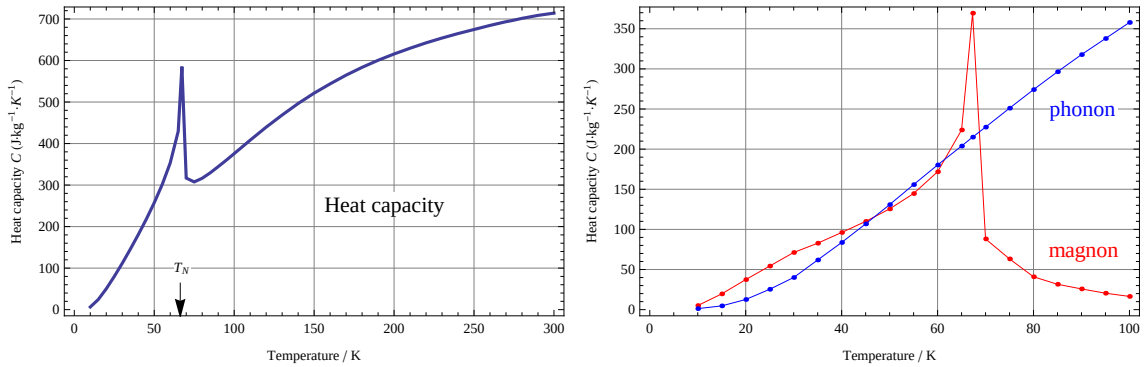

(a) total heat capacity **(b)** extracted phonon and magnon heat capacities

Figure 3.2: Heat capacity of MnF_2, taken from [9]. Néel temperature T_N is indicated by an arrow. Note that below transition temperature, magnon heat capacity is roughly the same compared to phonon's.

Thermal conductivity of MnF_2 is given in reference [18], and re-plot in figure 3.3. As shown in the figure, the conductivities increases almost exponentially when temperature decreases from room temperature, and reaches the maxima around 15 K and then decreases rapidly towards 0 when approaching 0 temperature. We can see an isotropy between conductivity along c direction, $\kappa_{\parallel}$ and that perpendicular to c, $\kappa_{\perp}$. $\kappa_{\parallel}$ is always slightly larger than $\kappa_{\perp}$. The ratio

between the two ranges from 1.4 at room temperature to about 1.5 at near 100 K, and to almost unity near zero temperature. To obtain heat conductivity along arbitrary direction, one can calculate equation 2.5.

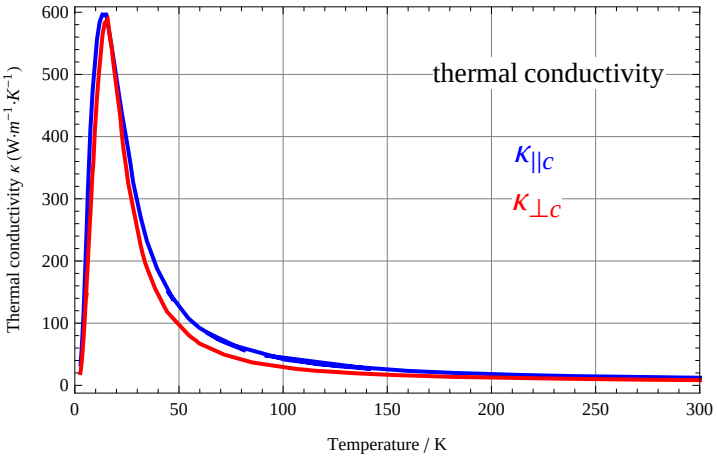

Figure 3.3: Thermal conductivities along (blue) or perpendicular to (red) c direction, of MnF_2, taken from [18]. Note that in this static measurement, very little or no magnon contribution was observed.

For magnetic contribution to total thermal conductivity, almost no magnon conductivity was present in such statically measured results even near T_N where magnon fluctuation is critical. This absence was attributed to a very long magnon-phonon relaxation time τmp in MnF_2 [7].

With heat capacity and thermal conductivity data, we can calculate the directly measured variable, thermal diffusivity α using $\alpha = \kappa/(\rho C)$. The result is depicted in figure 3.4.

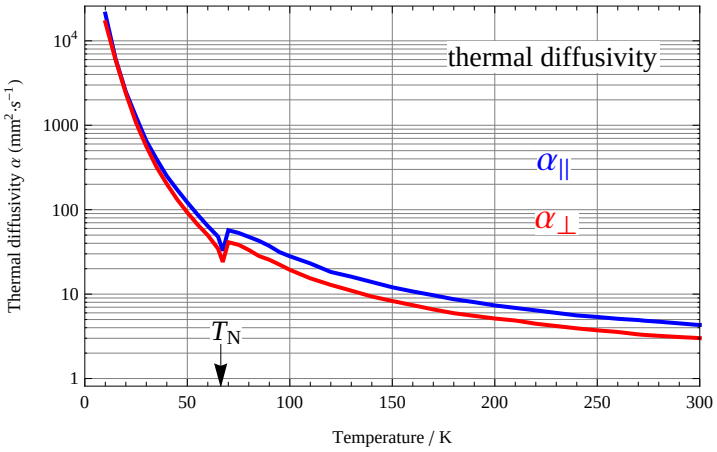

Figure 3.4: Thermal diffusivity of MnF_2 along (blue) or perpendicular to (red) c direction, calcualted from measured thermal conductivity and heat capapcity.

3.2 Fluorescent flash method

We use fluorescent flash method (FFM) to measure the thermal diffusivity and heat capacity of the sample. Like traditional flash method, a short laser pulse is impinged upon one side of the sample, and the temperature transient of the other side is recorded by a temperature sensor. In FFM, the temperature sensor we chose is a thin layer of polymer containing certain rare earth chelate compounds which show temperature dependent photoluminescence.

3.2.1 Flash method to measure thermal diffusivity

Laser flash techniques was developed by Parker *et al* [3] to measure the thermal diffusivity. A thermally isolated small slab-shaped sample is heated up by a short pulse of laser homogeneously on the front side, heating up electrons in a thin layer, the absorption depth. Then heat is quickly transfered to phonons through electron-phonon interactions. As the hot phonons diffuse around the sample, the back side gradually get heated up also, where temperature vs. time is recorded, as illustrated in figure 3.5. After obtaining the curve $\Delta T(t)$, we calculated thermal diffusivity of

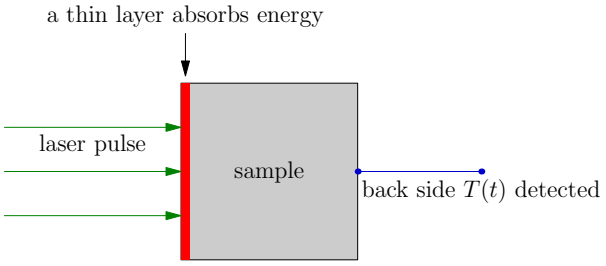

Figure 3.5: Illustration of laser flash method to measure thermal diffusivity.

the sample by fitting $\Delta T(t)$ to Parker's formula 2.11 or calculating from the half time $t_{\frac{1}{2}}$ 2.13.

Usually a μs duration laser pulse is short enough to heat up a thin layer instantaneously while temperature transient curve usually have a half time in millisecond scale for millimeter thick samples. For better absorption of laser pulse energy, a graphite thin layer is often applied on the front side of the sample. The back side temperature can be detected either using an infrared temperature sensor, a thermal couple, or more favorably a thin layer of temperature sensitive fluorophores.

The advantages of such laser flash technique include the ability to measure small samples and relative short measurement time. Causes of system error of such technique may include: inhomogeneous laser pulse, bad thermal contact of graphite with sample, heat loss to environment. For an overview, see references [19] and [20].

3.2.2 Detecting temperature using fluorophores

In this work, we apply on the back side of the sample a thin layer of polymer containing rare-earth chelate fluorophores EuTTA or EuTFC, whose luminescence is used as temperature sensor.

Europium thenoyltrifluoroacetonate (EuTTA) and europium tris[3-(trifluoro-methylhydroxy-methylene)-(+)-camphorate] (EuTFC) are organic chelate compound of rare earth metal europium (Eu). The structures of the two molecules are shown in figure 3.6. These compounds

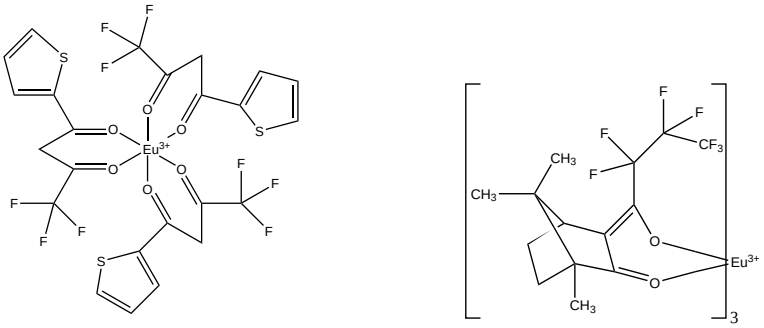

Figure 3.6: chemical structures of EuTTA and EuTFC.

are fluorophores absorbing in the UV and emitting around 612 nm. The absorption is due to the organic part, while the emission corresponds to the transition from $^5D_0$ level to ground state ^7F manifold of Eu^{3+} ion. The temperature dependence of the quantum efficiency can be briefly explained as following. Upon absorption of UV photons by the organic ligands (TTA or TFC), the organic part is elevated to a singlet excited state (step 1), following by intersystem crossing to a triplet state (step 2). The triplet state is a trap for the organic part since the transition from the triplet excited state to the singlet ground state is dipole forbidden. However, energy transfer can happen between the triplet state of the organic ligands and Eu^{+3} ion, exciting the rare earth ion to a fluorescing excited state $^5D_0$ (step 3). Finally photons are emitted during the radiative transition from $^5D_0$ to ground state manifold of Eu^{+3} ion (step 4), among which the transition $^5D_0 \rightarrow^7 F_2$ ($\sim$ 610 nm) is dominant [21]. For these four steps, the efficiency of step 3 is temperature dependent, because of e.g. non-radiative decay processes, whose rate is dependent on temperature.

Also quite interesting is that the polymer matrix also plays a role in the temperature dependence of the photoluminescence intensity. It is shown that for EuTTA, using poly(methyl methacrylate) (PMMA) or perdeutero-poly(methylmethacrylate) (dPMMA) has a factor of 2 difference in temperature sensitivity of the fluorescence [22].

Measured absorption and emission spectra of EuTTA and EuTFC are plot in figure 3.7.

From the measurements, we see for both materials a broad absorption peak in the UV, and a

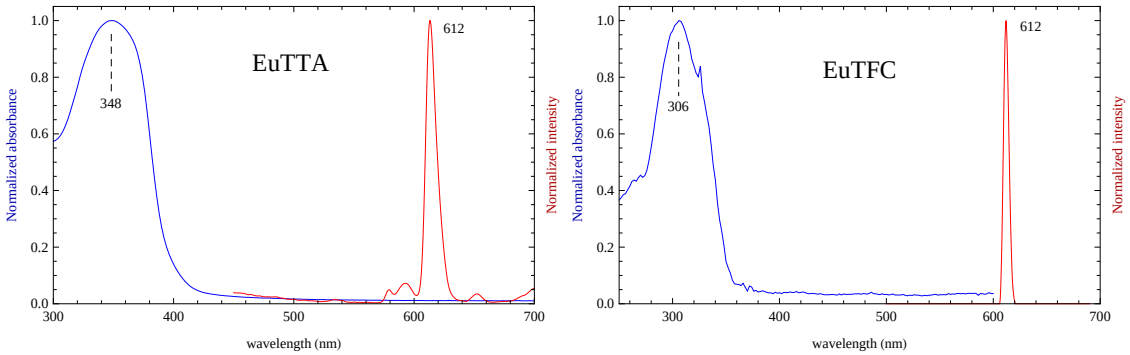

Figure 3.7: Absorption and emission spectra of EuTTA (left) and EuTFC (right). Samples are spincoated polymer films on quartz slides, with EuTTA in dPMMA, and EuTFC in PS. Absorption peaks are broad peaks sitting at 348 nm for EuTTA, and 306 nm for EuTFC; emission peaks are both very sharp and both at 612 nm.

sharp emission peak at same postions 612 nm. The positions of absorption peaks for EuTTA ($\sim$348 nm) and EuTFC ($\sim$306 nm) are quite different, which makes perfect sense since two different organic ligands absorbs differently.

Moreover, the quantum efficiency of these dyes are monotonically dependent on temperature, resulting in temperature dependent photoluminescence intensity under constant excitation power.

3.2.3 Fluorescent flash method

In 1982, Kolodner and Tyson developed a method of surface thermal imaging using EuTTA as a temperature sensor, and observed temperature resolution of 0.01°C and spatial resolution of 15 μm [23]. Since then, this method has been expanded to several other europium or other rare earth based fluorophores [24] , and to lower temperature down to 4.2 K using EuTFC [25].

In our measurements, we deposit a thin layer of fluorophore doped polymer onto the back side of the sample, and detect the fluorescence intensity as a measure of temperature. The setup is illustrated in figure 3.8 [26]. Laser pulses with wavelength $\lambda = 1064$ nm, duration around $\sim 60\mu$s and energy $\sim$ 60mJ is produced by a YAG laser, which can also generate 532 nm laser pulses with duration of 5 ns using second harmonic generation and a Q switch. Sample is sandwiched by Teflon plates mounted on top of a cold finger placed in a optical cryostat (Oxford Instruments). UV excitation source is a UV LED producing 360 nm light using intensity $\sim$ 20mW/cm^2 (1 mW in power) for EuTTA, or for EuTFC a fiber guided 300 nm laser source from the third harmonic of a Ti:Sapphire laser producing roughly the same intensity as the LED. Fluorescence signal is

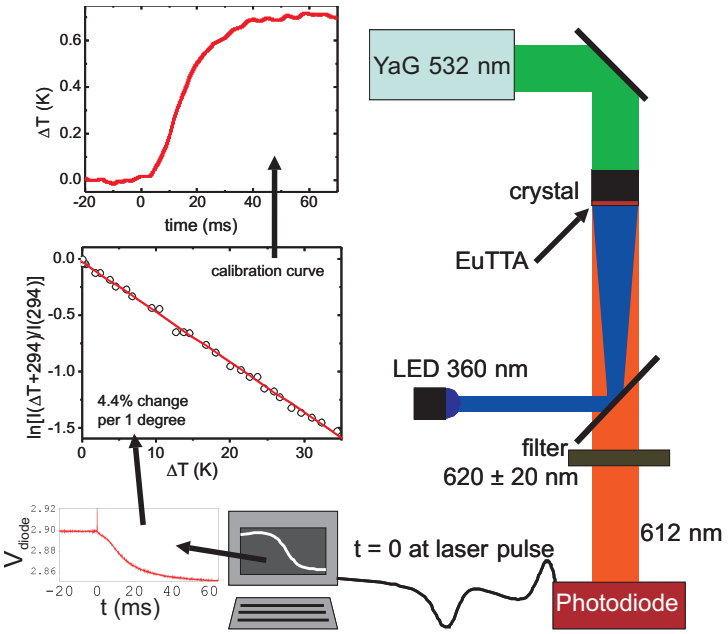

Figure 3.8: Setup of fluorescent flash method measurement. Sample is heated by a YAG laser, fluorescence of EuTTA or EuTFC layer is detected by a GaAsP photodiode. Measured fluorescence vs. time curve is converted to temperature vs. time using calibrated intensity of the fluorophore at different temperatures.

collected, filtered using a 610±10 nm interference filter and detected by a GaAsP photodiode. Liquid helium needs to be used for temperature below T_N.

To convert the measured fluorescence intensity to temperature change, we calibrated our temperature sensors, EuTTA or EuTFC, by measuring the fluorescence signal at different temperatures. To get convenient conversion, one can define the parameter "sensitivity" β as the relative change in intensity $V(T)$ per unit change of temperature,

$$\beta := \frac{\Delta V}{V} \Big/ \Delta T \simeq \frac{\Delta \ln V}{\Delta T} = \frac{\ln \frac{V_{\text{hot}}}{V_{\text{cold}}}}{\Delta T}\,, \tag{3.1}$$

where $V_{\text{hot}} = V(T + \Delta T)$ and $V_{\text{cold}} = V(T)$ are the intensities at slightly two different temperatures. This means the sensitivity is nothing but the slope of the curve $\ln V(T)$ *vs.* T. After obtaining sensitivity from calibration, we convert intensity to temperature rise, one can rewrite equation 3.1 as

$$\Delta T = \frac{1}{\beta} \ln \frac{V_{\text{hot}}}{V_{\text{cold}}}\,. \tag{3.2}$$

An typical calibration curve for EuTTA from 70 K to 300 K is shown in figure 3.9. As shown in the figure, the fluorescence intensity increases when temperature is lowered, dropping very fast from 300 to 200 K, and almost saturated below 100 K. While sensitivity decreases as temperature decreases, from roughly $3\%{\cdot}\text{K}^{-1}$ around room temperature, to $\sim 0.1\%{\cdot}\text{K}^{-1}$ at 70 K.

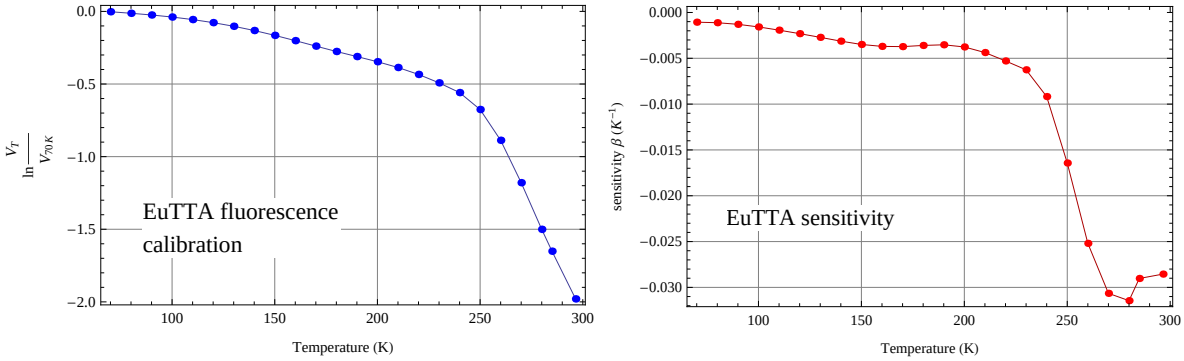

(a) Logrithmic intensity *vs.* temperature

(b) Sensitivity *vs.* temperature

Figure 3.9: Measured calibration curve for a EuTTA/dPMMA layer between 70 K and 300 K. Sensitivity is roughly $-3\% \cdot \mathrm{K}^{-1}$ around room temperature, and $\sim -0.1\% \cdot \mathrm{K}^{-1}$ at 70 K. Data taken from [26].

For EuTFC, polystyrene (PS) was used instead of dPMMA due to better performance [26]. Similar sensitivity behavior for EuTFC/PS was observed, however the sensitivity drops more slowly at low temperatures, yielding typically -0.6∼-1%·K^{-1} in temperature range 60 K to 120 K, much larger than EuTTA in the sample temperature region. Thus we selected EuTTA for room temperature measurements and EuTFC for low temperature.

3.2.4 Sample preparation

MnF_2 samples are kept in a desiccator to keep away from water. Several pieces of MnF_2 samples with same orientation, different thicknesses vary from 0.5 mm to 2 mm and area around $2{\times}2\,\mathrm{mm}^2$ were cut using a diamond wire saw and polished to obtain a brick shape.

EuTTA/dPMMA layer was spincoated on one side of the sample using a mixture solution of 3% (wt) dPMMA, 2% EuTTA in chlorobenzene. For EuTFC/PS, same weight ratio was used. A spinning speed of 400 rpm results in a polymer layer of $\sim 1\,\mu$m thick. After the layer was dried, sample was heated at 125°C for 30 min to solidify the polymer matrix to prevent delamination at low temperatures. Note that different incubation temperature and time might cause differences in sensitivities of the resulting polymer/fluorophore layer [25].

After heating, remnant fluorophore and polymer was removed carefully with acetone, preferably carried out under a microscope. On the front side of the sample, a thin layer of graphite was applied using a carbon spray. Finally the sample was mounted onto a cold finger by applying some sticky tape between sample edge and substrate. The substrate was made of Telfon covered copper plate for thermal isolation consideration. Sample holder was properly blocked to prevent laser light going through and reaching the detector.

Chapter 4

Results, Discussion and Conclusion

We used fluorescent flash method to measure the thermal conductivity of MnF_2 single crystal samples with different thicknesses, at room temperature and below Néel temperature. At each temperature, 30 curves were averaged to improve the signal-to-noise ratio.

4.1 Room temperature measurement

A typical temperature transient curve was plotted in figure 4.1. Experiment conditions of this data is: $T = 300\,\mathrm{K}$, thickness L =1.028 mm, averaging from 30 single curves. As we can see

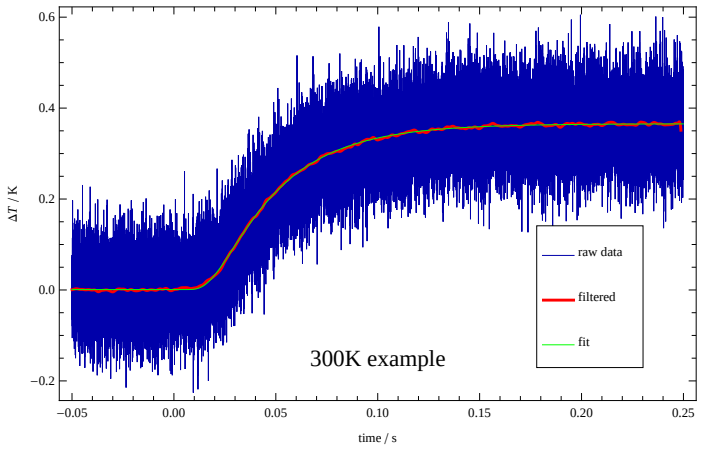

Figure 4.1: Typical measurement showing temperature rise $\Delta T(t) = T(t) - T(t_{\min})$ in K versus time in seconds. Blue colored is the raw data, red curve is Fourier filtered of blue, and the green curve is the fit of blue using 2.11. The RMS (root-mean-square) noise level of the measured curve is $\Delta T_{\mathrm{noise}} = 0.06\,\mathrm{K}$, signal (temperature rise) is $\Delta T \simeq 0.4\,\mathrm{K}$, resulting a signal-to-noise ration about 7.

from the figure, the back side temperature stays constant before $t = 0$ when a laser pulse hits

the front side of the sample. After time 0, back side temperature gradually increases and reach a plateau value corresponding to equilibrium temperature. Although in the raw data a high frequency noise is significant, the curve shows quite clear the typical behavior of a temperature transient curve 2.1. This is seen in the filtered curve. A fit curve produced by fitting the raw data (or filtered data) to theoretical curve 2.11 confirms that measured curve coincides with theoretical solution quite well.

Thermal diffusivity of this measurement can be obtained from fitting, giving $\alpha_{\text{measure}}(300\,\text{K})$= $3.38\pm0.04\,\text{mm}^2/\text{s}$. The error bar is estimated from fitting the raw data as well as the filtered curve, using different time intervals. The fit result is comparable from the one calculated from literature value $\alpha_{\text{literature}}(300\,\text{K}) = 3.6 \pm 0.2\text{mm}^2/\text{s}$. Uncertainty of the calculated values originates from the uncertainty of angle between c and heat flow direction ($\sim \pm5^\circ$) due to imperfect cutting, as well as from digitization of data from literature ($\sim \pm3\%$).

We have 4 different samples with the same orientation, thickness of each is listed in table 4.1. Room temperature results for 4 thicknesses are shown in figure 4.2.

Table 4.1: Thicknesses of 4 samples cut in parallel from the same piece.

sample No.	thickness (mm)	area size (mm^2)
1	0.532±0.002	2.6×2.2
2	1.028±0.002	2.6×2.1
3	1.255±0.002	2.6×1.6
4	1.965±0.002	2.6×2.1

As can be seen from the figure, the 4 temperature transient curves for 4 different thickness samples seems to be shifted horizontally from each other. We can do such a shift operation by normalizing horizontal axis by dividing the thickness squared of each sample $t \to t/L^2$, noting that dividing a constant in normal scale is equivalent to subtracting a constant in logarithm scale. The 4 curves after normalizing is shown in figure 4.2b.

Now 4 curves almost coincide with each other. Considering that $T(t/L^2)$ curve only depends thermal diffusivity α (as can be seen from 2.13), this means diffusivities of these 4 samples are the roughly the same. To confirm this, we fit 4 measured curves with Parker's formula 2.11 and obtained α for each sample, listed in table 4.2 and plotted in figure 4.3. To conclude our room temperature measurement results, for 4 different thicknesses we obtain roughly the same thermal diffusivity, independent on thickness of the sample. Also the measured values show no discrepancy with the predicted value $\alpha_{\text{literature}}(65\,\text{K}) = 3.6 \pm 0.2\,\text{mm}^2/\text{s}$ calculated from literature.

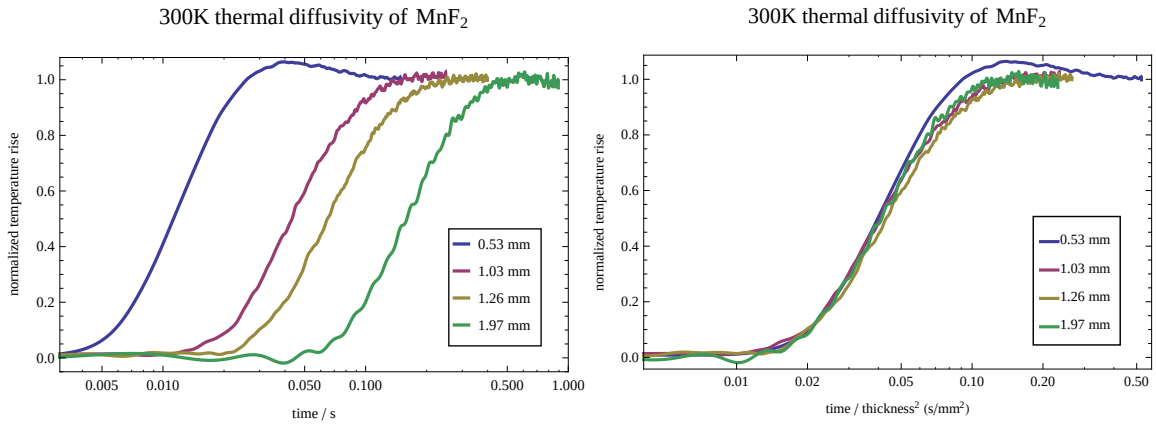

(a) $\Delta T(t)$ *vs.* t **(b)** $\Delta T(t)$ *vs.* t/L^2

Figure 4.2: Temperature transient curves (100 Hz filtered) for 4 different thicknesses, measured at room temperature (300 K). Sample thickness corresponding to each curve is listed in the legends. y axes represent normalized temperature rise $\Delta T(t)/\Delta T(t_{\max})$, while x axis in (**a**) shows time in seconds in logarithm scale, (**b**) shows time divided by thickness squared t/L^2.

Table 4.2: Measured thermal diffusivity of MnF_2 for 4 thicknesses, and maximum temperature rise $\Delta T(t_{\max})$ of each measurement.

thickness (mm)	diffusivity (mm^2/s)	$\Delta T(t_{\max})$ (K)
0.53	3.37±0.04	1.3
1.03	3.38±0.04	0.4
1.26	3.35±0.04	0.5
1.97	3.44±0.08	0.3

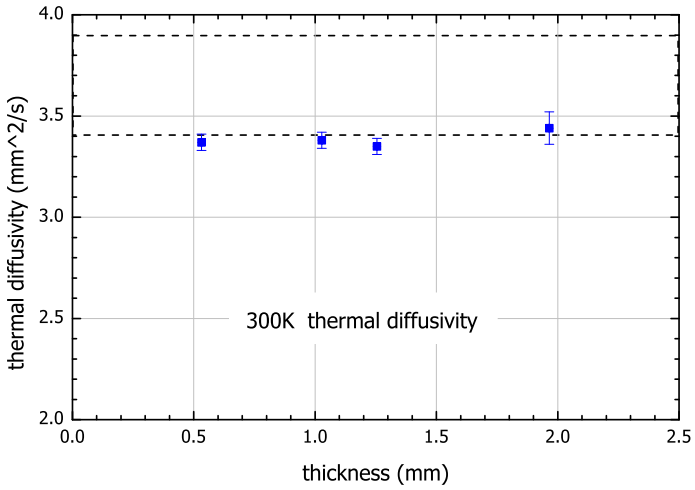

Figure 4.3: 300K measured diffusivity of MnF_2 samples of thickness 0.53, 1.03, 1.26, 1.97 mm. Blue squares show the measured values, while the 2 dashed lines represent calculated value range.

4.2 Low temperature measurements

At $T = 65\,\mathrm{K}$, just below Néel temperature, 3 samples, namely #1, #2 and #4 in table 4.1, were measured. An example of measured curve is shown in figure 4.4. Compared with room temperature measurements, measurements at 65 K has noise 3∼4 times larger. This is mainly due to less temperature sensitivity of the fluorophore and reduced overall fluorescence intensity due to usually less excitation power.

The $\Delta T(t)$ curves for three different thicknesses are shown in figure 4.5 . We see from the figure 4.5b that the 3 curves for different thicknesses differ from each other, since they are not likely superpositions to each other. The values of the 3 thermal diffusivities is listed in table 4.3, and plotted in figure 4.6.

Table 4.3: Measured thermal diffusivities of 3 thicknesses at temperature $T = 65\,\mathrm{K}$.

thickness (mm)	diffusivity (mm^2/s)	$\Delta T(t_{\max})$ (K)
0.53	5.5±0.4	0.6
1.03	6.8±0.4	1.0
1.97	18±2	0.4

The results show an evident thickness dependence of measured thermal diffusivity, i.e. for thicker sample α was larger, about 4 times difference for 0.53 mm and 1.97 mm samples. Also

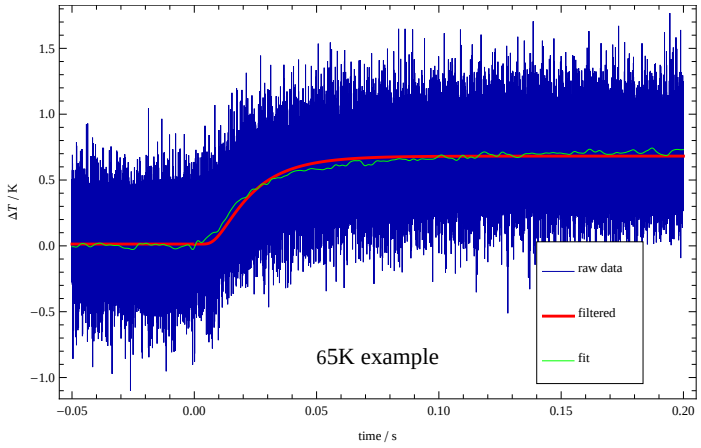

Figure 4.4: One example $T(t)$ curve measured at 65 K for 1.03 mm sample. Blue is raw data, averaging from 30 shots, green is 500 Hz filtered, red the fit. Noise level of the measured curve is $\Delta T_{\text{noise}} = 0.28\,\text{K}$, signal (temperature rise) is $\Delta T \simeq 0.6\,\text{K}$, signal-to-noise ratio about 2.

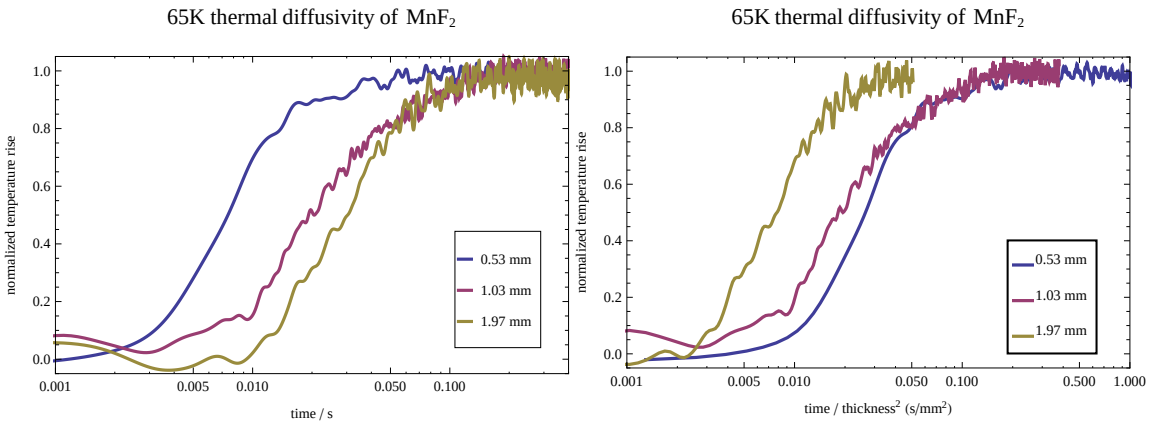

(a) $\Delta T(t)$ *vs.* t **(b)** $\Delta T(t)$ *vs.* t

Figure 4.5: $\Delta T(t)$ curves measured for 3 different thickness samples at temperature $T = 65\,\text{K}$. Sample thickness corresponding to each curve is listed in the legends. y axes represent normalized temperature rise $\Delta T(t)/\Delta T(t_{\max})$, while x axis in (**a**) shows time in seconds in logarithm scale, (**b**) shows time divided by thickness squared t/L^2.

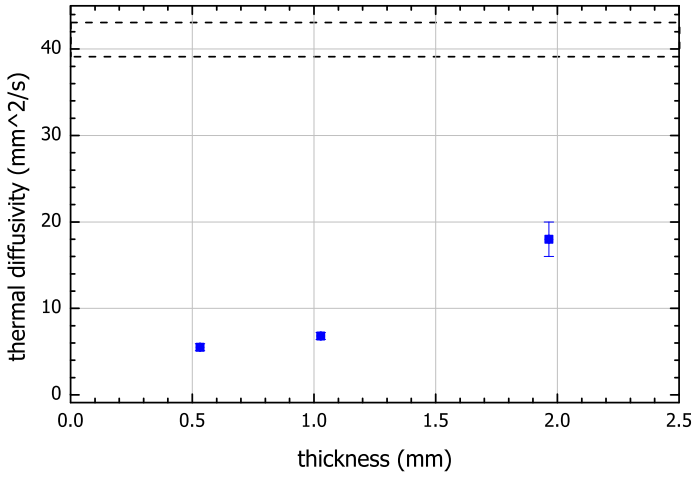

Figure 4.6: 65 K measured diffusivity of MnF_2 samples of thickness 0.53, 1.03, 1.97 mm. Blue squares show the measured values, while the 2 dashed lines represent calculated value range.

interesting is that even for the thickest sample in this series (1.97 mm sample), α_{measure} ($\simeq 18\,\text{mm}^2/\text{s}$) is still roughly 2 times smaller than predicted value $\alpha_{\text{literature}}(65\,\text{K}) = 41 \pm 2\,\text{mm}^2/\text{s}$ which is a steady state value from static measurements.

Compared to room temperature measurements, low temperature measurements suffer a bigger error. For room temperature, temperature sensitivity of the fluorophore EuTTA is much higher (3∼4%), thus better signal-to-noise ratio and smaller error. Low temperature measurements, temperature sensitivity of EuTFC is less than 1% and more difficult to excite (wavelength ∼300 nm), resulting measurement errors is 5 ∼ 10 times bigger. To improve the signal-to-noise ratio for low temperature measurement, one needs to optimize the sensitivity of the fluorophore by exploring different preparation conditions, using different polymer matrices or different dyes. One can also increase the excitation (UV) power however this will in the meantime increase the photobleaching of the fluorophore, resulting in a non-constant baseline.

4.3 Discussion and conclusion

At room temperature where magnons do not contribute to heat transport, FFM measured thermal diffusivity (thus thermal conductivity) shows no thickness dependence and good agreement to steady state value; at 65 K which is below Néel temperature where magnons should be important in heat transport, the measured thermal diffusivity for 3 thicknesses exhibits an strong thickness dependence and a possibly significant deviation from steady state value. Although one needs more data for even thicker samples, it's highly possible that even for largest thickness limit the measured diffusivity would still be much smaller than static value.

The thickness dependence as well the anomaly at low temperature is a strong indication of long magnon-phonon thermalization time τ_{mp} as shown by previously experiments on spin ladder compound $Ca_9La_5Cu_{24}O_{41}$ [8], where $\tau_{\mathrm{mp}} \sim 400\,\mu$s. Similar to the case of spin ladders, we might attribute the discrepancy in thermal diffusivity of MnF_2 to the broken points in the magnetic structures, for instance magnetic impurities or domain walls between domains.

We can also try to estimate τ_{mp} by fitting the 65 K results for 3 thicknesses using 2.23.The result is depicted in figure 4.7with fitting parameters of each curve listed in table 4.4. Unfortunately using experimental data for C_l, C_m and κ_l as fixed values and varying only κ_m and τ_{mp} does not produce a good fit, as shown as dashed curve in the figure. So we have to change C_m, κ_m and/or κ_l also to obtain better fits, as shown by blue, green and brown curves.

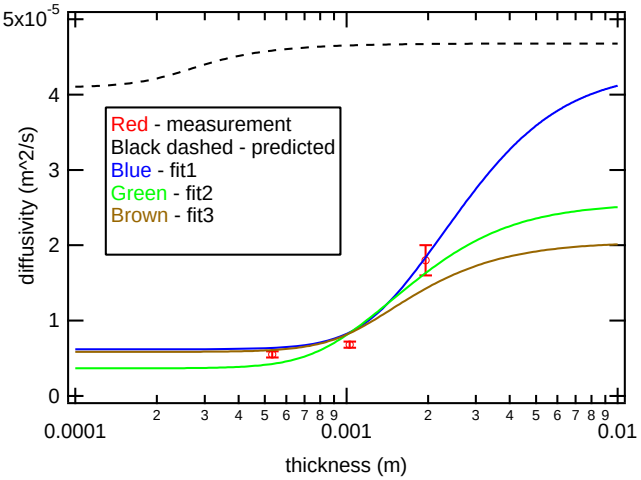

Figure 4.7: Fitting (blue, green and brown curves) of thermal diffusivity vs. thickness of the measurement result. Parameters corresponding to each curve is listed in table.

Table 4.4: Fitting parameters for each curve shown in figure 4.7

curve	C_m/C_l	$\kappa_l(\mathrm{W}\cdot\mathrm{m}^{-1}\cdot\mathrm{K}^{-1})$	$\kappa_m(\mathrm{W}\cdot\mathrm{m}^{-1}\cdot\mathrm{K}^{-1})$	τ_{mp} (s)
predicted	~ 1	70	10	N.A.
1	1/100	5	30	4×10^{-4}
2	1/100	3	18	3.5×10^{-4}
3	1	10	25	0.01

As seen from the figure, in order to have a good fit, thermal conductivity of magnons needs to be larger than that of phonons. This suggests a much smaller phonon thermal conductivity compared with previous measurements. Also suggested from the fits (blue and green curves) is that in order to have a magnon-phonon thermalization time in the order of 10^{-4} s, the thermal

capacity of magnon needs to be roughly 100 times smaller than phonon, which also contradicts with previous static measurements. This might be true if only part of the whole population of magnons is contributing to heat transport. If one insists a comparable heat capacity from magnons, instead, the thermalization time τ_{mp} is around 0.01 s, roughly 2 orders of magnitude too large compared to literature value. In total, this effort of trying to fit the data indicates that there's still something happening there beyond our present understanding.

In order to make to show more clearly the dependence on thickness at low temperature, as well as to make a more accurate estimation of τ_{mp}, more measurements need to be done, especially on thicker samples. To achieve that, one needs to minimized the uncertainty in the measurements for very thick samples (better thermal isolation needed) as well for very thin samples (better homogeneity of laser beam needed, since effect of inhomogeneous laser heat has been seen in the overshooting of thin sample curve).

In conclusion, thermal diffusivity of MnF_2 with different thicknesses ranging from $\sim$0.5 mm to $\sim$2 mm have been measured at both 300 K and 65 K. While at room temperature, the results show no thickness dependence and similar value compared to static measurement; at 65 K thermal diffusivity shows a strong thickness dependence (4 times difference between 0.5 mm and 2 mm samples) as well as an indication of deviation from steady state value. In the future, more measurements with thicker samples needed to be done in order to grasp more details on thickness dependence and discover the possible deviation from static value, as well as a better estimation of the magnon-phonon relaxation time in MnF_2.

Bibliography

[1] Yoshitami Ajiro. ESR experiments on quantum spin systems. *Journal of the Physical Society of Japan*, 72SB(Supplement B):12–25, 2003.

[2] S. Notbohm, P. Ribeiro, B. Lake, D. A. Tennant, K. P. Schmidt, G. S. Uhrig, C. Hess, R. Klingeler, G. Behr, B. Büchner, M. Reehuis, R. I. Bewley, C. D. Frost, P. Manuel, and R. S. Eccleston. One- and two-triplon spectra of a cuprate ladder. *Phys. Rev. Lett.*, 98:027403, Jan 2007.

[3] W. J. Parker, R. J. Jenkins, C. P. Butler, and G. L. Abbott. Flash method of determining thermal diffusivity, heat capacity, and thermal conductivity. *Journal of Applied Physics*, 32(9):1679–1684, 1961.

[4] J. W. Che, T. Cagin, W. Q. Deng, and W. A. Goddard. Thermal conductivity of diamond and related materials from molecular dynamics simulations. *Journal Of Chemical Phsyics*, 113(16):6888, 2000.

[5] R. E. Newnham. *Properties Of Materials: Anisotropy, Symmetry, Structure.* Oxford University Press, 2005.

[6] H. S. Carslaw and J. C. Jaeger. *Conduction of heat in solids.* Oxford science publications. Clarendon Press, 1986.

[7] D. J. Sanders and D. Walton. Effect of magnon-phonon thermal relaxation on heat transport by magnons. *Phys. Rev. B*, 15:1489–1494, 1977.

[8] M. Montagnese, M. Otter, N. Hlubek, O. Mitiashkin, C. Hess, R. Saint-Martin, S. Singh, A. Revcolevschi, and P. H. M. van Loosdrecht. Phonon-magnon interaction in low dimensional quantum magnets observed by dynamic heat transport measurements. in review, 2012.

[9] W. O. J. Boo and J. W. Stout. Heat capacity and entropy of mnf_2 from 10 to 300°K. evaluation of the contributions associated with magnetic ordering. *The Journal of Chemical Physics*, 65(10):3929–3934, 1976.

[10] J. Gustafson and C. T. Walker. Thermal conductivity in two simple antiferromagnets: $RbMnF_3$ and MnF_2. *Phys. Rev. B*, 8:3309–3322, Oct 1973.

[11] J. W. Stout and Stanley A. Reed. The crystal structure of MnF_2, FeF_2, CoF_2, NiF_2 and ZnF_2. *Journal of the American Chemical Society*, 76(21):5279–5281, 1954.

[12] Z. Yamani, Z. Tun, and D. H. Ryan. Neutron scattering study of the classical antiferromagnet mnf2: a perfect hands-on neutron scattering teaching course. *Canadian Journal of Physics*, 88(10):771–797, 2010.

[13] D. P. Belanger, A. R. King, and V. Jaccarino. Temperature dependence of the optical birefringence of mnf_2, mgf_2, and znf_2. *Phys. Rev. B*, 29:2636–2643, 1984.

[14] I. R. Jahn. Linear magnetic birefringence in the antiferromagnetic iron group difluorides. *physica status solidi (b)*, 57(2):681–692, 1973.

[15] S. P. S. Porto, P. A. Fleury, and T. C. Damen. Raman spectra of tio_2, mgf_2, znf_2, fef_2, and mnf_2. *Phys. Rev.*, 154:522–526, 1967.

[16] D. J. Lockwood and M. G. Cottam. Light scattering from magnons in mnf_2. *Phys. Rev. B*, 35:1973–1982, 1987.

[17] Noriko Akutsu and Hironobu Ikeda. Specific heat capacities of CoF_2, MnF_2 and $KMnF_3$ near the Néel temperatures. *Journal of the Physical Society of Japan*, 50(9):2865–2871, 1981.

[18] Glen A. Slack. Thermal conductivity of CaF_2, MnF_2, CoF_2, and ZnF_2 crystals. *Phys. Rev.*, 122:1451–1464, 1961.

[19] M. Sheindlin, D. Halton, M. Musella, and C. Ronchi. Advances in the use of laser-flash techniques for thermal diffusivity measurement. *Review of Scientific Instruments*, 69(3):1426–1436, 1998.

[20] L. M. Clark III and R. E. Taylor. Radiation loss in the flash method for thermal diffusivity. *Journal of Applied Physics*, 46(2):714–719, 1975.

[21] J. Pantoflíček and L. Parma. The luminescence properties of SmD and EuTTA. *Czechoslovak Journal of Physics*, 18:1610–1621, 1968.

[22] P. R. Kolodner. Method and apparatus for measuring the temperature profile of a surface, 1989.

[23] Paul Kolodner and J. Anthony Tyson. Microscopic fluorescent imaging of surface temperature profiles with 0.01°C resolution. *Applied Physics Letters*, 40(9):782–784, 1982.

[24] P. R. Kolodner. Fluorescent thermal imaging using rare-earth chelate films, 1999.

[25] Ø. Haugen and T.H. Johansen. Temperature dependent photoluminescence down to 4.2°K in eutfc. *Journal of Luminescence*, 128(9):1479 – 1483, 2008.

[26] Marian Otter. *Magnetic heat transport in low-dimensional quantum magnets*. PhD thesis, University of Groningen, 2012.